



Deep Synoptic Array Science: First FRB and Host Galaxy Catalog

Casey J. Law^{1,2,4} , Kritti Sharma^{1,4} , Vikram Ravi^{1,2} , Ge Chen¹ , Morgan Catha², Liam Connor¹ , Jakob T. Faber¹, Gregg Hallinan^{1,2} , Charlie Harnach², Greg Hellbourg^{1,2} , Rick Hobbs², David Hodge¹, Mark Hodges², James W. Lamb² , Paul Rasmussen², Myles B. Sherman¹ , Jun Shi¹ , Dana Simard¹ , Reynier Squillace^{1,3} , Sander Weinreb¹, David P. Woody², and Nitika Yadlapalli Yurk¹

¹ Cahill Center for Astronomy and Astrophysics, MC 249-17 California Institute of Technology, Pasadena, CA 91125, USA; claw@astro.caltech.edu

² Owens Valley Radio Observatory, California Institute of Technology, Big Pine, CA 93513, USA

³ Steward Observatory, University of Arizona, 933 N. Cherry Avenue, Tucson, AZ 85721, USA

Received 2023 July 6; revised 2024 January 12; accepted 2024 March 21; published 2024 May 15

Abstract

Fast radio bursts (FRBs) are a powerful and mysterious new class of transients that are luminous enough to be detected at cosmological distances. By associating FRBs to host galaxies, we can measure intrinsic and environmental properties that test FRB origin models, in addition to using them as precise probes of distant cosmic gas. The Deep Synoptic Array (DSA-110) is a radio interferometer built to maximize the rate at which it can simultaneously detect and localize FRBs. Here, we present the first sample of FRBs and host galaxies discovered by the DSA-110. This sample of 11 FRBs is the largest, most uniform sample of localized FRBs to date, as it is selected based on association with host galaxies identified in optical imaging by Pan-STARRS1. These FRBs have not been observed to repeat, and their radio properties (dispersion, temporal scattering, energy) are similar to that of the known nonrepeating FRB population. Most host galaxies have ongoing star formation, as has been identified before for FRB hosts. Two hosts of the new sample are massive, quiescent galaxies. The distribution of star formation history across this host-galaxy sample shows that the delay time distribution is wide, with a power-law model that spans from ~ 100 Myr to $\gtrsim 2$ Gyr. This requires the existence of one or more progenitor formation channels associated with old stellar populations, such as the binary evolution of compact objects.

Unified Astronomy Thesaurus concepts: [Radio transient sources \(2008\)](#); [Radio telescopes \(1360\)](#); [Galaxies \(573\)](#)

1. Introduction

Fast radio bursts (FRBs) are a new class of $\ll 1$ s radio transient that is powerful enough to be seen from distant galaxies (Cordes & Chatterjee 2019; Petroff et al. 2022). The nature of the source (or sources) that make FRBs is not known yet. Several hundred bursts have been detected (CHIME/FRB Collaboration et al. 2021), some of which repeat stochastically (Chime/FRB Collaboration et al. 2023) and some of which burst with quasiperiodic patterns over a wide range of timescales (Chime/FRB Collaboration et al. 2020a; Pastor-Marazuela et al. 2023). Polarimetric measurements have identified dynamic, highly magnetized plasma in the parsec-scale environments of some FRB sources (Anna-Thomas et al. 2023; Mckinven et al. 2023).

The need to localize FRBs to an arcsecond (or better) precision has motivated a new generation of radio instruments (e.g., Macquart et al. 2010; Law et al. 2018; Sanidas et al. 2018; van Leeuwen et al. 2023). Of the roughly two dozen localized FRBs, the story told by their host galaxies and host environments is confusing. Most FRBs are associated with actively star-forming galaxies (Chatterjee et al. 2017; Mannings et al. 2021; Bhandari et al. 2022), consistent with the discovery of FRB-like bursts from a magnetar in our own galactic disk (Bochenek et al. 2020; CHIME/FRB Collaboration et al. 2020b). However, some FRBs have been associated with much older stellar systems, including a nearby globular cluster (Kirsten et al. 2022) and a quiescent

galaxy (Sharma et al. 2023). A small fraction has a compact, persistent radio source (PRS) that is coincident with the FRB, but many other FRBs have strict limits on such emission (Marcote et al. 2020; Law et al. 2022; Niu et al. 2022). Therefore, a concordant picture of the FRB progenitors has not yet emerged from studies of FRB hosts.

A major question raised with the discovery of FRBs remains unanswered: what source (or sources) produces these powerful bursts? Their occurrence rate ($\sim 10^5$ Gpc $^{-3}$ yr $^{-1}$ for burst energy $> 10^{39}$ erg Hz $^{-1}$; Ravi 2019; James et al. 2022) is too high to be attributed solely to cataclysmic events such as classes of supernovae (SNe). Models based on magnetized neutron stars can reproduce many burst properties and FRB associations (Zhang 2020). However, even this one kind of object can be formed in young (through core-collapse SNe) or older (through compact binary coalescence) stellar environments (Margalit et al. 2019; Kremer et al. 2021). Some FRB behaviors, such as quasiperiodic activity timescales, have been used to argue that binarity plays a role (Chime/FRB Collaboration et al. 2020a; Lyutikov et al. 2020; Li et al. 2023). Finally, as proposed in Gordon et al. (2023) and Sharma et al. (2023), multiple formation channels may exist and be associated with specific stellar environments, as is the case for SNe (Perley et al. 2020; Lu et al. 2022) and gamma-ray bursts (GRBs; Woosley & Bloom 2006; Berger 2014). If so, then a large sample of FRB host galaxy associations and careful statistical analysis will be required to identify specific classes of FRB source and their formation channels.

Here, we present the first sample of FRBs discovered by the Deep Synoptic Array (DSA-110). This sample was selected from FRB discoveries made during science commissioning from 2022 February to October. We selected all FRBs that are

⁴ These authors contributed equally to this work.



associated with a host galaxy in Pan-STARRS1, which we used to guide follow-up optical spectroscopic and IR photometric observations. This sample represents a significant increase in the number of FRBs with quality host galaxies identified over the last 7 yr (e.g., Tendulkar et al. 2017; Marcote et al. 2020; Bhandari et al. 2022; Rajwade et al. 2022). Three FRBs included in this sample have been reported in other publications (FRBs 20220319D, 20220509G, 20220914A; Ravi et al. 2023a; Connor et al. 2023; Sharma et al. 2023) and this work uses the same instrument and analysis techniques described previously.

Our goal is to present a host magnitude-limited sample of FRBs and their host galaxies to probe ideas for FRB origin (see Section 2). The DSA-110 was in science commissioning during this observing period, so the overall observing efficiency is not measured well enough to estimate an FRB rate. However, the FRB characterization and host identification are reliable enough to use this sample to study burst phenomenology and galaxy properties (see Section 3). In Section 4, we discuss the details of FRB host galaxies and how their star formation history is most consistent with FRB sources formed over a wide range of delay times. This is supported by analysis of the nearest FRBs and hosts, for which we have more reliable host identification and high physical resolution. We conclude in Section 5 by discussing FRB origins and whether multiple models are required. We adopt standard cosmological parameters from Planck Collaboration et al. (2020).

2. Observations

2.1. DSA-110

DSA-110 is built to discover, localize, and characterize FRBs. The first FRB localization by the instrument demonstrated the techniques used for the current sample (Ravi et al. 2023a). A full description of the DSA-110 interferometer and FRB search system will be presented in V. Ravi et al. (2024, in preparation).

FRBs described here were detected during science commissioning with an array of sixty-three, 4.65 m antennas distributed over a 2.5 km area at the Owens Valley Radio Observatory.⁵ The FRB search system uses 48 antennas arranged as a linear array to form 256 coherent *fan beams* spaced by $1'$, thus spanning a little beyond the primary beamwidth of 3.4° (FWHM). DSA-110 is a transit telescope with motorized control over antenna elevation. During all observations described here, the array was pointed at a decl. of $71^\circ 6'$.

The digital and software systems search a continual stream of calibrated power beams in real time for FRBs. The FRB search is designed to avoid and remove radio frequency interference (RFI) by pointing away from known RFI sources, automatically suspending the search during RFI *storms* and data cleaning. The search system is optimally sensitive to temporal widths from 0.26–8.32 ms, and FRB-like dispersion measures (DMs) of 50 – 1500 pc cm⁻³. For the fixed decl. of the observations, the instrument observed Galactic latitudes from 8° – 46° , which corresponds to a Milky Way DM contribution ranging from 133 – 36 pc cm⁻³ (Cordes & Lazio 2002).

The search system is designed to automatically identify FRBs based on several criteria. The significance of power excess in any beam must be greater than 8.5 and not associated

with strong terrestrial interference, and have a DM greater than both 50 pc cm⁻³ and 0.75 times the Galactic DM contribution. For each candidate FRB, the system saves metadata, and channelized voltage data from the entire array (48 search antennas and 15 outrigger antennas). The voltage data can fully reproduce the real-time search data, as well as enable fine localization, high time and frequency resolution, and full polarimetry. Verification of each candidate is ultimately reliant on a successful interferometric localization.

Table 1 and Figure 1 present the first sample of 11 FRBs detected by DSA-110 and robustly associated with counterparts detected by Pan-STARRS1 (Section 2.3). These events were identified during science commissioning from 2022 January to October. Analysis of this sample is presented in Section 3.1. A more detailed analysis of the burst properties, including full polarimetry, is presented in Sherman et al. (2023, 2024) and G. Chen et al. (2024, in preparation). DSA-110 FRB detections, including data to aid in reproducing this analysis, are available on the DSA-110 archive⁶ and in the FRB software and data repository (Prochaska et al. 2023).

2.2. Pan-STARRS1

Figure 2 shows Pan-STARRS1 (PS1; Chambers et al. 2016) *gri* imaging of the likely FRB host galaxies. PS1 provides images and catalogs for the entire sky north of a decl. of -30° (the “3pi Steradian Survey”). Multi-epoch image stacks reach a depth of 21–23 mag (5σ) with a median seeing from $1''.3$ – $1''.0$ in the *g*, *r*, *i*, *z*, and *y* bands.

DSA-110 localizes FRBs with a precision better than roughly $\pm 2''$ at 90% confidence, which corresponds to 3.8 kpc at a redshift of 0.1. This resolution is similar to the half-light radius of a typical galaxy (e.g., Shen et al. 2003). Thus, in many cases, DSA-110 FRBs can be associated with individual galaxies at the characteristic distance of the FRB population. However, by requiring robust association with PS1, we introduce an optical magnitude limit to the FRB host sample. Selection requires that the host be detected in the *r* and *i* bands above the 5σ detection limits of 23.2 and 23.1 mag, respectively.

2.3. Associating FRBs with Host Galaxies

Table 2 summarizes the properties of the host galaxies used to associate them with the FRBs. We use *astropath* (Aggarwal et al. 2021) to calculate the probability of association for each FRB with its host galaxy. The Bayesian framework estimates the probability of association for all nearby galaxies from the FRB position and error, as well as galaxy magnitude, location, and size. Galaxies with a probability of association greater than 0.9 are considered robust, given the conservative assumptions, and thus included in this sample.

We use the adopted priors in Aggarwal et al. (2021), defined as an exponential FRB angular offset distribution and a probability of association that scales inversely to the number density of galaxies at a given magnitude (“exp” and “inverse,” respectively). We deviate from the adopted set of *astropath* priors by using a nonzero prior on undetected host galaxies, $P(U)$. Seebeck et al. (2021) analyzed the false-positive and false-negative association rates for simulated FRB host galaxies. At the depth of PS1 *r*-band imaging, a reliable and accurate probability of association is found for $P(U) = 0.2$. All 11 FRBs

⁵ See <https://www.ovro.caltech.edu>.

⁶ <http://code.deepsynoptic.org/dsa110-archive>

Table 1
The First Sample of DSA-110 FRBs Listed in Order of Discovery, with Both Formal and Informal Names in the First Column

FRB Name	Time (MJD)	Location (J2000) (arcsec)	S/N	Fluence (Jy ms)	DM (pc cm ⁻³)	DM _{ISM} (pc cm ⁻³)	Width (ms)
20220207C/“Zach”	59617.808504	20 ^h 40 ^m 47. ^s 886, +72 ^h 52 ^m 56. ^s 378 (0.63, 0.54)	60.0	16.2	262.38 0.01	79.3	0.5
20220307B/“Alex”	59645.845634	23 ^h 23 ^m 29. ^s 88, +72 ^h 11 ^m 32. ^s 6 (1.72, 1.26)	11.9	3.2	499.27 0.06	135.7	0.5
20220310F/“Whitney”	59648.241721	8 ^h 58 ^m 52. ^s 9, +73 ^h 29 ^m 27. ^s 0 (1.9, 1.4)	68.4	26.2	462.24 0.005	45.4	1.0
20220319D/“Mark”	59657.932757	02 ^h 08 ^m 42. ^s 70, +71 ^h 02 ^m 06. ^s 9 (0.58, 0.55)	41.7	8.0	110.98 0.02	133.3	0.3
20220319D/“Mark”	59657.932757	02 ^h 08 ^m 42. ^s 70, +71 ^h 02 ^m 06. ^s 9 (0.58, 0.55)	41.7	8.0	110.98 0.02	133.3	0.3
20220418A/“Quincy”	59687.355728	14 ^h 36 ^m 25. ^s 34, +70 ^h 05 ^m 45. ^s 4 (1.356, 0.761)	10.9	4.2	623.25 0.01	37.6	1.0
20220506D/“Oran”	59705.597013	21 ^h 12 ^m 10. ^s 76, +72 ^h 49 ^m 38. ^s 2 (1.11, 0.81)	48.9	13.2	396.97 0.02	89.1	0.5
20220509G/“Jackie”	59708.4944990805	18 ^h 50 ^m 40. ^s 8, +70 ^h 14 ^m 37. ^s 8 (2.2, 1.5)	21.5	5.8	269.53 0.02	55.2	0.5
20220825A/“Ansel”	59816.2572924694	20 ^h 47 ^m 55. ^s 55, +72 ^h 35 ^m 05. ^s 9 (0.78, 0.69)	15.1	5.8	651.24 0.06	79.7	1.0
20220914A/“Elektra”	59836.145966	18 ^h 48 ^m 13. ^s 63, +73 ^h 20 ^m 12. ^s 9 (0.93, 0.73)	9.6	2.6	631.28 0.04	55.2	0.5
20220920A/“Etienne”	59842.9815705163	16 ^h 01 ^m 01. ^s 70, +70 ^h 55 ^m 07. ^s 7 (1.02, 0.60)	14.4	3.9	314.99 0.01	40.3	0.5
20221012A/“Juan”	59864.0510912293	18 ^h 43 ^m 11. ^s 69, +70 ^h 31 ^m 27. ^s 2 (1.12, 0.74)	9.4	5.1	441.08 0.7	54.4	2.0

Note. Time is topocentric and referenced to the top of the observing band at 1530 MHz. Position errors are listed on alternate rows. Location error is quoted as 1σ uncertainties (statistical + systematic). The DM and width maximize the signal-to-noise ratio (S/N) of the brightest component; width corresponds to a temporal boxcar size. Fluence is measured from high-resolution data to contain 90% of the flux density. The DM_{ISM} is measured from the model of Cordes & Lazio (2002).

are covered by Pan-STARRS1 DR2, but six of the FRBs are covered by the deeper Legacy Survey DR9 (Dey et al. 2019). For FRBs covered by the Legacy Survey, we use $P(U) = 0.1$.

For each FRB, we build a galaxy catalog from PS1 stack images or Legacy catalogs by selecting resolved sources within $30''$ (117 kpc at the median redshift of this sample; see Table 3). For PS1, pointlike sources are removed if they are in the PS1-PSC catalog with a “ps_score” less than 0.83 (Tachibana & Miller 2018). No compactness filter was used for Legacy Survey sources, but all FRB host galaxies are resolved, with $R_e > 1''$. For PS1, we use the r -band Kron radius to represent the galaxy’s size, which is within 20% of the half-light radius under realistic scenarios (Graham & Driver 2005). We find a probability of association much greater than 0.9 for all FRBs presented in Table 2.

2.4. Optical/IR Photometry

Appendix Table 4 summarizes the photometric and spectroscopic measurements made and used in the modeling of host galaxies. We use catalog photometry from wide-area optical/IR surveys PS1, Two Micron All Sky Survey (2MASS; Skrutskie et al. 2006), and ALLWISE (Cutri et al. 2021) surveys. We also acquired IR photometric data in J and H bands with the Wide Field Infrared Camera (WIRC; Wilson et al. 2003) observing instrument mounted on the Palomar 200 inch Telescope. These observations were acquired on 2022 August 16, and were reduced by a custom pipeline following the standard data reduction pipeline procedures. We largely follow the analysis framework established in Sharma et al. (2023) to characterize the host galaxies of these FRBs

(including the removal of a star on the host galaxy of 20220509G). We convert the Vega magnitudes to AB magnitudes and correct for galactic dust extinction.

2.5. Optical/IR Spectroscopy

With a reliable host identified, we observed each galaxy with optical/IR spectroscopic instruments. Detection of line emission allows accurate redshift measurement and line flux estimates to better understand the nature of ongoing star formation and nuclear activity, and to model the ages of the stellar populations in a galaxy. The age of the stellar population of an FRB host galaxy tells us about how star formation creates FRB sources, a crucial test of origin models. Appendix Table 4 summarizes the spectroscopic instruments used for this FRB sample.

We observed with the Low-Resolution Imaging Spectrometer on the Keck I telescope (Keck I/LRIS Oke et al. 1995) on May 26, July 21, and October 17 of 2022. The light was dispersed using a 300/5000 *grism* to measure a detector-frame wavelength range from 3450–6700 Å. The spectra were reduced with the standard `lpipe` software (Perley 2019) and calibrated using observations of the standard star BD+28 4211. The spectrum was scaled to match the PS1 photometry to account for slit losses.

We observed with the Double Spectrograph (DBSP; Oke & Gunn 1982) mounted on the Palomar Hale 200 inch telescope on 2022 June 1 and December 12, and 2023 May 28. Data were reduced following procedures described in Ravi et al. (2022).

We measure the spectroscopic redshift and the line fluxes of the host galaxies using the penalized PiXel-Fitting software (`pPXF`; Cappellari 2017, 2023) by jointly fitting the stellar

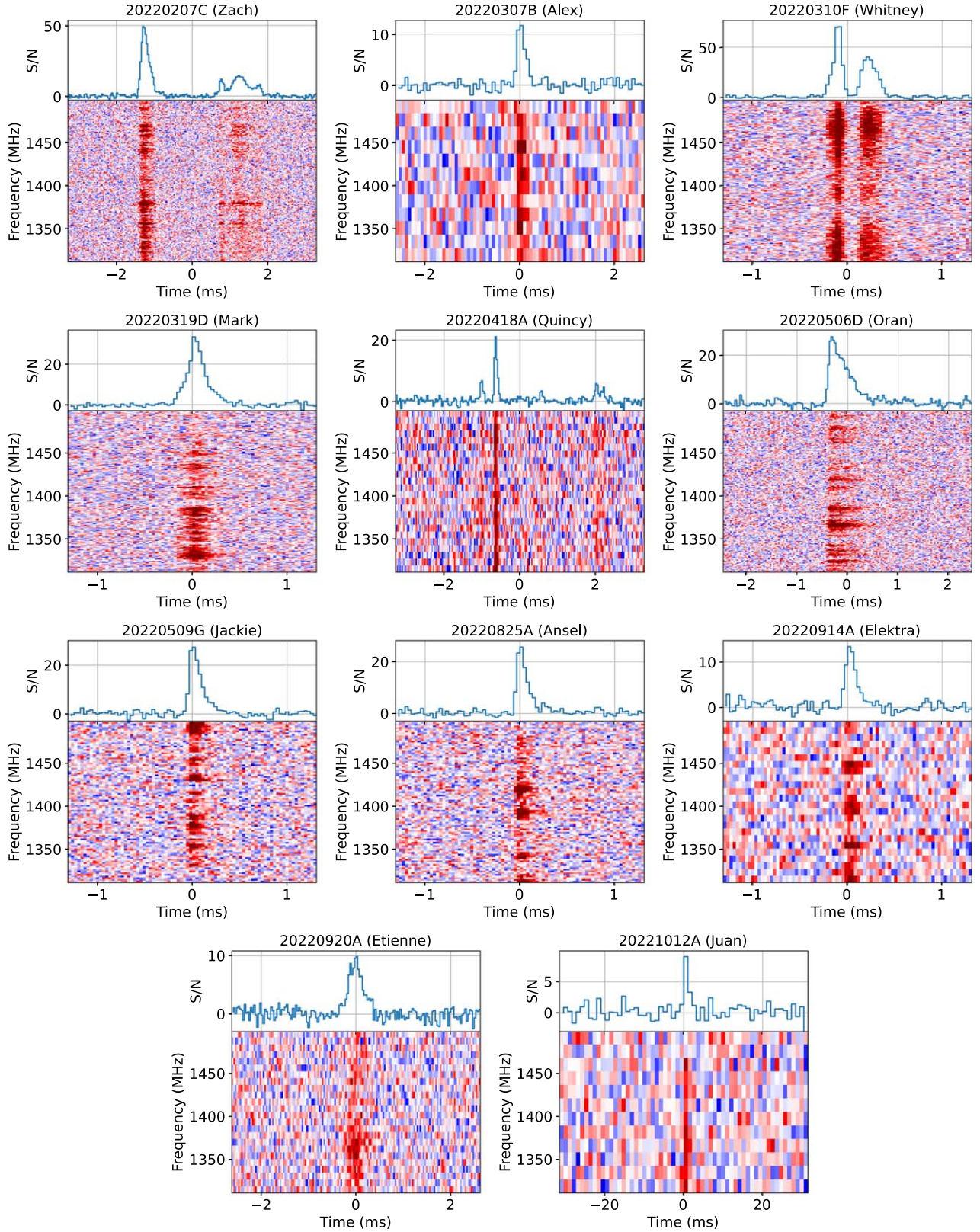


Figure 1. Dynamic spectra for DSA-110 FRB discoveries, listed in order of discovery. The color map shows the power in the tied-array beam, while the top panel shows the frequency-averaged light curve in units of S/N. (Top row) Plots for FRBs 20220207C, 20220307B, and 20220310F. (Second row) Plots for FRBs 20220319D, 20220418A, and 20220506D. (Third row) Plots for FRBs 20220509G, 20220825A, and 20220914A. (Bottom Row) FPlots for RBs 20220920A and 20221012A.

continuum and nebular emission using the MILES stellar library (Sánchez-Blázquez et al. 2006). The line fluxes are shown in [Appendix Table 5](#). A redshift could be reliably

identified for all hosts by the detection of at least three emission lines. For one FRB, 20220509G, we measured the redshift by modeling absorption lines.

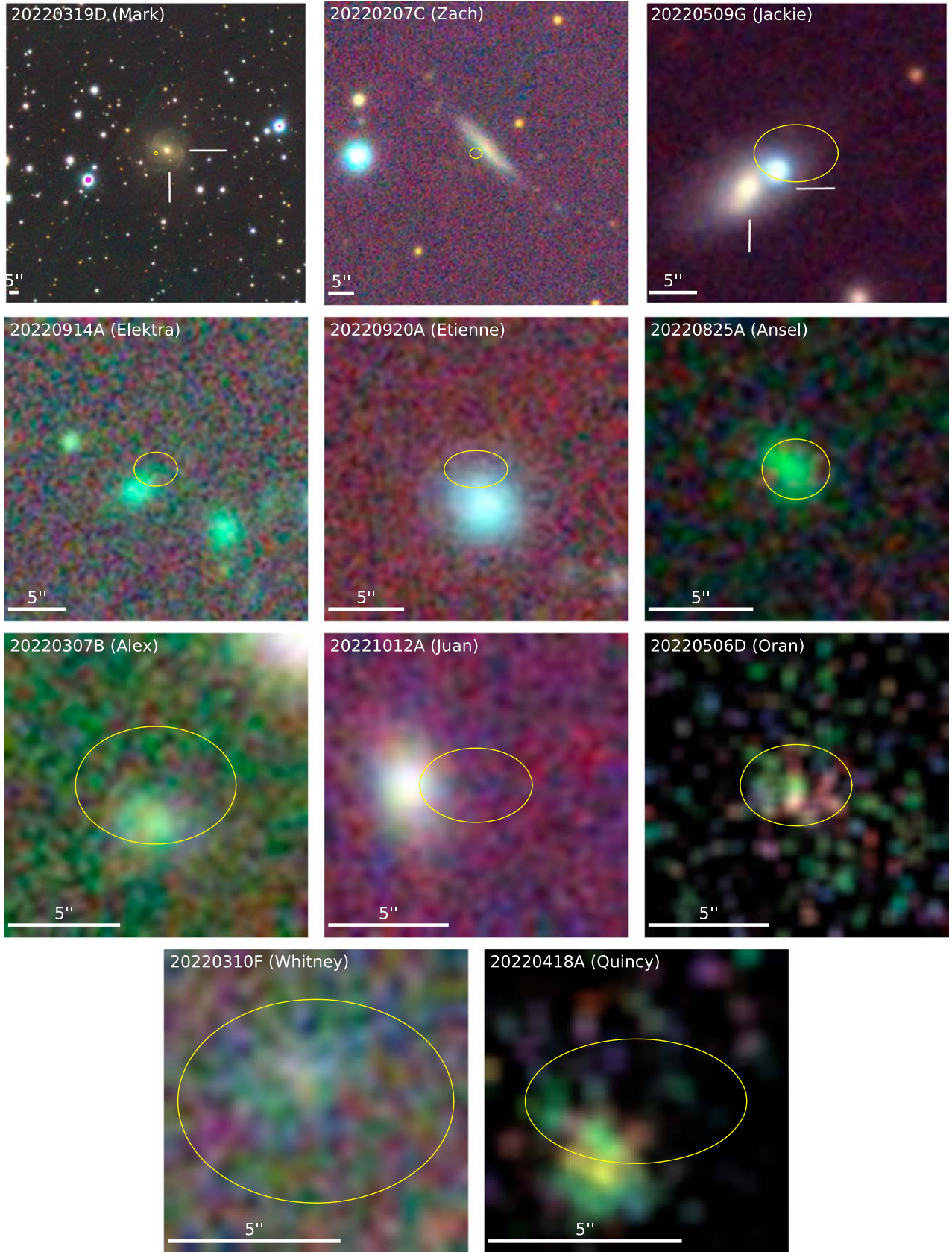


Figure 2. Fixed-scale Pan-STARRS1 images of FRB host galaxies in order of distance (see Table 3). Each image is scaled to span a fixed horizontal size of 60 kpc. The yellow circle shows the FRB localization uncertainty region (90% confidence). (Top row) Plots for FRBs 20220319D, 20220207C, and 20220509G. For two of these, we identify the host galaxy with crosshairs. (Second row) Plots for FRBs 20220914A, 20220920A, and 20220825A. (Third row) Plots for FRBs 20220307B, 20221012A, and 20220506D. (Bottom row) Plots for FRBs 20220310F and 20220418A.

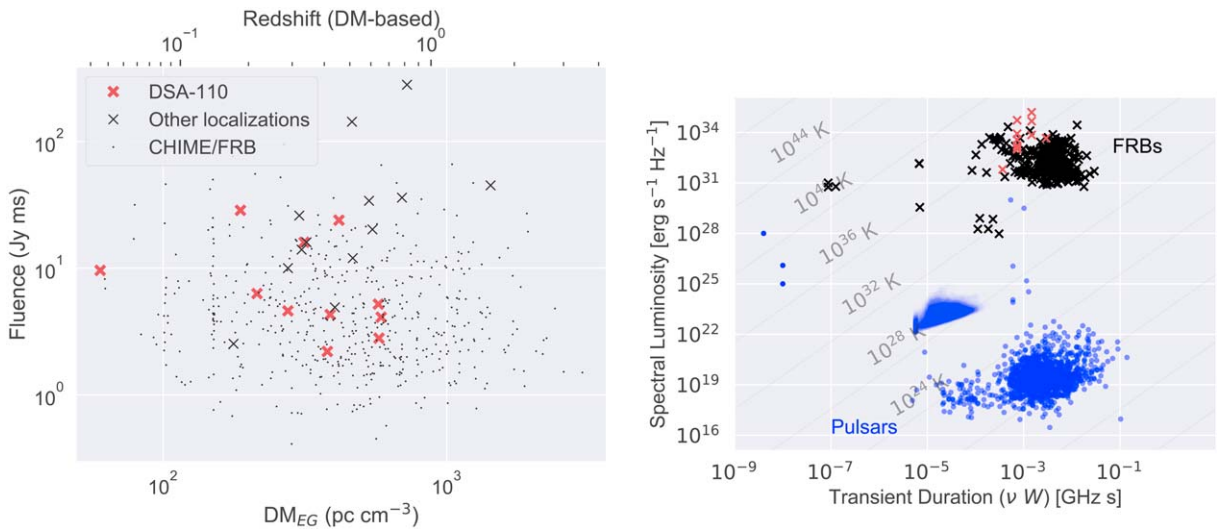


Figure 3. (Left) Burst DM vs. fluence for a sample of DSA-110 (red crosses), other localized events (black crosses), and CHIME-FRB detections (black points; CHIME/FRB Collaboration et al. 2021). The scale of DM to redshift assumes linear conversion with a Milky Way halo contribution of 30 and 850 pc cm^{-3} to a redshift of 1. (Right) Luminosity vs. timescale for Galactic (blue circles) and extragalactic (black crosses) fast transients. The DSA-110 FRB sample is shown as red crosses.

2.6. Radio and High-energy Counterpart Search

Two FRBs have been associated with PRS and another has been associated with a known high-energy source (a magnetar). We searched for new examples of these associations by matching FRB positions to wide-area radio and X-ray catalogs. The focus was on compact counterparts, which are simpler to characterize and associate with pointlike FRB emission. Radio catalogs with coverage of this decl. range include VLASS (Lacy et al. 2020), NVSS (Condon et al. 1998), TGSS (Intema et al. 2017), GB6 (Gregory et al. 1996), WeNSS (Rengelink et al. 1997), VLSSr (Lane et al. 2014), and LoTSS (Shimwell et al. 2019). At high energies, we searched the Chandra Source Catalog 2 (“csc21_snapshot_scs”; Evans et al. 2020) and XMM/Newton 4XMM-DR11 (Webb et al. 2020). No counterpart was found for any of our samples in these catalogs. Radio limits are fairly heterogeneous and range from approximately 1 mJy to tens of millijansky over frequencies from 120 MHz to 5 GHz. X-ray limits. Most FRBs had no coverage in high-energy catalogs.

As the nearest nonrepeating FRB, the environment and counterparts to 20220319D can be probed especially well. We observed 20220319D with the Karl G. Jansky Very Large Array (VLA) under program 22A-490 to search for PRS and repeat bursts. We observed with antennas in the A configuration in the 1.4 and 5 GHz bands. The correlator was configured for continuum observing and a commensal 10 ms transient search with the *realfast* instrument (Law et al. 2018). We detected no burst or persistent counterpart and the continuum imaging sensitivity was approximately $21 \mu\text{Jy beam}^{-1}$ in both bands (1σ , dual-polarization, robust weighting).

3. Analysis

3.1. Burst Properties

The radio bursts themselves can be used to constrain both intrinsic properties and propagation effects. Bursts are characterized by DM, intrinsic width and structure, scintillation, scattering, as well as polarimetric properties. For the total-intensity burst properties considered here, we find that the DSA-110 sample is typical of the nonrepeating population identified previously.

Figure 3 shows the extragalactic DM compared to burst fluence for DSA-110 and other FRB discoveries. The new sample has a median fluence of $\sim 5 \text{ Jy ms}$, compared to $\sim 20 \text{ Jy ms}$ for the reference sample of localized FRBs with data available in Prochaska et al. (2023). This reflects the improved sensitivity of DSA-110 relative to other localization instruments (dominated by ASKAP).

Figure 3 also shows the luminosity and timescale distribution for Galactic and extragalactic millisecond transients (see Nimmo et al. 2022). The present sample is somewhat shorter and more luminous than the bulk of previous detections. This offset reflects the sensitivity and relatively fast sampling time of the DSA-110 search system. We note that the requirement for a PS1 host biases against very distant hosts and high FRB luminosities. Future FRB samples from DSA-110 with dedicated follow-up optical observing should be expected to show higher burst luminosities.

Of special interest is whether bursts repeat or have a complex *substructure* within individual bursts. Using the burst classification defined in Pleunis et al. (2021), we characterize eight bursts as *broad* and three as *complex*. These terms are synonymous with having single or multiple millisecond-scale components in time, respectively. We note that the relatively fast time resolution and relatively narrow bandwidth of DSA-110 make it easier for DSA-110 to detect and identify bursts as complex, while limiting the ability to see narrow or downward drifting bursts. A more complete discussion of burst classification with the inclusion of polarimetric properties is presented in Sherman et al. (2024), and a detailed analysis of the total-intensity properties will be presented in G. Chen et al. (2024, in preparation).

None of the bursts were observed to repeat on timescales longer than a second. Based on the observing pattern during the science commissioning period, the FRB locations were nominally observed for 150 hr through the 2022 observing year.⁷ If the three multicomponent bursts were treated as repeat bursts, then the wait times range from 0.5–3 ms. This is consistent with the first peak of the wait time distribution for active repeating FRBs such as 121102 (Li et al. 2021).

⁷ The effective observing time is currently not well constrained, so no rate estimate can be calculated.

Table 2
Parameters of DSA-110 FRB Host Galaxies Listed in Order of Discovery

FRB Name	Host Name	Host R.A. (J2000)	Host Decl. (J2000)	m_r (mag)	r_e (arcsec)	Source	P_{host}
20220207C	PSO J310.1977+72.8826	20 ^h 40 ^m 47. ^s 419	+72°52′57. [″] 90	16.15 ± 0.01	8.356	P	0.99
20220307B	PSO J350.8747+72.1918	23 ^h 23 ^m 29. ^s 925	+72°11′30. [″] 80	20.45 ± 0.05	1.393	P	0.99
20220310F	PSO J134.7211+73.4910	08 ^h 58 ^m 53. ^s 054	+73°29′27. [″] 45	21.20 ± 0.08	1.909	P	0.99
20220319D	IRAS 02044+7048	02 ^h 08 ^m 40. ^s 812	+71°02′09. [″] 65	13.25 ± 0.01	11.764	P	0.99
20220418A	PSO J219.1065+70.0953	14 ^h 36 ^m 25. ^s 584	+70°0′43. [″] 60	22.22 ± 0.20	1.290	L	0.97
20220506D	PSO J318.0447+72.8272	21 ^h 12 ^m 10. ^s 727	+72°49′37. [″] 76	19.91 ± 0.16	2.425	P	0.98
20220509G	PSO J282.6748+70.2427	18 ^h 50 ^m 41. ^s 916	+70°14′33. [″] 95	16.51 ± 0.01	3.938	L	0.99
20220825A	PSO J311.9820+72.5848	20 ^h 47 ^m 55. ^s 6	+72°35′06. [″] 5	19.36 ± 0.16	1.935	P	1.0
20220914A	PSO J282.0585+73.3363	18 ^h 4 ^m 13. ^s 958	+73°20′10. [″] 70	20.05 ± 0.04	1.278	L	0.97
20220920A	PSO J240.2568+70.9180	16 ^h 01 ^m 01. ^s 634	+70°55′05. [″] 05	19.46 ± 0.03	2.116	L	0.99
20221012A	PSO J280.8014+70.5242	18 ^h 43 ^m 12. ^s 3	+70°31′27. [″] 2	19.67 ± 0.03	3.096	L	1.0

Note. The columns include information used to identify and associate the galaxy to the FRB, including r -band magnitude and effective radius, r_e . P_{host} is the astrophysical posterior probability of association of the galaxy to the FRB. The field “source” describes what catalog was used to search for potential counterparts, with “P” for Pan-STARRS1 and “L” for Legacy Survey. P_{host} refers to the probability that the FRB is associated with this galaxy (see Section 2.3).

Table 3
Measured and Derived Properties of the DSA-110 FRB Host Galaxies with FRBs Listed in Order of Discovery

FRB Name	Redshift	M_r (mag)	$g - r$ (mag)	$\log(M_*)$ (M_\odot)	$\text{SFR}_{100\text{Myr}}$ ($M_\odot \text{ yr}^{-1}$)	t_m (Gyr)	L_{PRS} ($\text{erg s}^{-1} \text{ Hz}^{-1}$)
20220207C	0.043040	$-20.20^{+0.01}_{-0.00}$	$0.30^{+0.01}_{-0.00}$	$9.91^{+0.03}_{-0.02}$	$1.16^{+0.10}_{-0.08}$	$6.53^{+0.84}_{-0.72}$	$<2.3 \times 10^{28}$
20220307B	0.248123	$-19.97^{+0.00}_{-0.00}$	$0.85^{+0.01}_{-0.01}$	$10.04^{+0.02}_{-0.01}$	$2.71^{+0.76}_{-0.61}$	$0.65^{+0.04}_{-0.04}$	$<1.0 \times 10^{30}$
20220310F	0.477958	$-20.79^{+0.03}_{-0.03}$	$0.99^{+0.06}_{-0.05}$	$9.97^{+0.05}_{-0.05}$	$4.25^{+2.45}_{-1.67}$	$2.13^{+1.06}_{-0.60}$	$<4.6 \times 10^{30}$
20220319D	0.011228	$-20.23^{+0.01}_{-0.01}$	$0.46^{+0.03}_{-0.02}$	$10.16^{+0.03}_{-0.06}$	$0.21^{+0.12}_{-0.05}$	$6.30^{+1.51}_{-1.82}$	$<1.8 \times 10^{26a}$
20220418A	0.622000	$-20.88^{+0.01}_{-0.01}$	$0.64^{+0.04}_{-0.03}$	$10.31^{+0.06}_{-0.05}$	$29.41^{+18.28}_{-10.70}$	$4.62^{+1.20}_{-0.98}$	$<8.6 \times 10^{30}$
20220506D	0.30039	$-20.63^{+0.01}_{-0.01}$	$1.50^{+0.03}_{-0.03}$	$10.29^{+0.06}_{-0.07}$	$5.08^{+0.31}_{-0.47}$	$0.07^{+0.02}_{-0.01}$	$<1.5 \times 10^{30}$
20220509G	0.089400	$-21.34^{+0.00}_{-0.00}$	$0.78^{+0.00}_{-0.00}$	$10.79^{+0.01}_{-0.01}$	$0.23^{+0.04}_{-0.03}$	$9.03^{+0.46}_{-0.42}$	$<1.1 \times 10^{29}$
20220825A	0.241397	$-19.46^{+0.07}_{-0.02}$	$0.87^{+0.06}_{-0.16}$	$9.95^{+0.17}_{-0.15}$	$1.62^{+0.47}_{-0.31}$	$3.46^{+1.49}_{-1.02}$	$<9.4 \times 10^{29}$
20220914A	0.113900	$-18.31^{+0.02}_{-0.02}$	$0.52^{+0.03}_{-0.02}$	$9.48^{+0.07}_{-0.09}$	$0.72^{+0.20}_{-0.15}$	$7.50^{+1.86}_{-1.50}$	$<1.8 \times 10^{29}$
20220920A	0.158239	$-19.96^{+0.02}_{-0.01}$	$0.48^{+0.02}_{-0.01}$	$9.81^{+0.08}_{-0.04}$	$4.10^{+1.09}_{-1.00}$	$3.86^{+1.56}_{-0.89}$	$<3.6 \times 10^{29}$
20221012A	0.284669	$-20.94^{+0.01}_{-0.01}$	$1.50^{+0.01}_{-0.01}$	$10.99^{+0.02}_{-0.02}$	$0.15^{+0.04}_{-0.03}$	$6.75^{+0.56}_{-0.41}$	$<1.4 \times 10^{30}$

Note. t_m refers to the mass-weighted age of the galaxy’s stellar population. See the Appendix for model fit plots. Limit on persistent radio counterparts derived from the VLA Sky Survey at 3 GHz, except where noted.

^a Dedicated VLA follow-up at 1.4 and 5 GHz.

3.2. Host Galaxy Spectral Energy Distribution Modeling

We obtain the stellar properties of our set of host galaxies using the stellar population synthesis modeling software *Prospector* (Johnson et al. 2021). We follow the spectral energy distribution (SED) modeling approach described in Sharma et al. (2023), which includes a discussion of spectral processing, model parameters, and priors. In brief, we simultaneously fit a model to the spectrophotometric data. The redshift is initialized to the value measured with pPXF and given a uniform prior width of 1%. We use a continuity nonparametric star formation history with seven bins and the Chabrier initial mass function. We add an active galactic nucleus (AGN) component to the model whenever data above $2 \mu\text{m}$ is available. We sample from the posterior using the ensemble sampler *emcee* (Foreman-Mackey et al. 2013).

Generally, the photometric and flux-calibrated spectroscopic observations are jointly fit when possible. Spectroscopy toward host galaxies of 20220207C, 20220506D, and 20220319D had poor quality, so channels were selected around line emission for inclusion in SED modeling. For 20220418A, we use

Legacy Survey data instead of PS1 in our SED modeling, due to the better signal-to-noise ratio (S/N) in Legacy data. The resulting SED fits for all the host galaxies, along with their constrained nonparametric star formation histories, are displayed in Appendix Figures 8–9, and 10–11, respectively. The set of derived host properties is summarized in Table 3 and plotted in Figure 4. Best-fit line fluxes measured by pPXF are shown in Appendix Table 5. We note that the recent star formation history is not well constrained in a few cases. We suspect that this is primarily due to the lack of UV photometry in our SED modeling.

3.3. Limits on PRSs

PRS have been robustly associated with two FRBs (Tendulkar et al. 2017; Niu et al. 2022) and have been a valuable driver of models for the physics of FRBs (e.g., Margalit & Metzger 2018). Law et al. (2022) present a phenomenological definition of a PRS as a compact (subparsec), luminous ($L_r > 10^{29} \text{ erg s}^{-1} \text{ Hz}^{-1}$) radio source that is spatially coincident with an FRB. Given this definition, they were able to

provide a more homogenous analysis of the PRS population and how they may be causally connected to FRBs. Note that this luminosity limit is defined phenomenologically to exclude astrophysical foregrounds and that nondetections do not necessarily rule out the physical object that produces PRS-like emission.

We find no persistent radio counterparts associated with these DSA-110 FRBs. The VLASS 3σ limit is 0.5 mJy (at 3 GHz). Using the PRS luminosity threshold proposed previously, we can exclude the presence of a PRS in FRBs 20220207C and 20220319D. FRBs 20220509G, 20220506D, and 20220914A are slightly above the limit, but still fainter than the two confirmed PRS.

We reviewed recently published FRB localizations to build on the sample of known PRS and upper limits (Caleb et al. 2023; Gordon et al. 2023; Ravi et al. 2023a; Ryder et al. 2023; Driessen et al. 2024). Among new localizations from ASKAP and MeerKAT, we find that nonrepeating FRBs 20211212A, 20211127I, 20210405I, and 20210410D all have significant constraints on PRS counterparts. The FRBs presented in Rajwade et al. (2022) have less robust associations with host galaxies and Chibueze et al. (2022) include a PRS candidate that may be attributed to star formation in its host galaxy, so they are not counted here.

Considering these new PRS constraints from DSA-110, MeerKAT, and ASKAP, we find 15 nonrepeating FRBs with upper limits on PRS counterparts. The measurements toward repeating FRBs remain unchanged, with two detections out of six useful measurements. Repeating the analysis of Law et al. (2022), we lower the 90% upper limit on the fraction of nonrepeating FRBs with a PRS at 0.14, and find an 8% chance that the repeater and nonrepeater PRS fraction are consistent with each other. We conclude that there is weak evidence for repeating FRBs to be associated with PRS. We encourage more radio imaging of localized FRBs to understand whether PRS and repetition have a causal relationship.

4. Discussion

4.1. What Kind of Galaxies Host FRBs?

Analysis of a population of FRB host galaxies can provide insights into formation and evolution channels. We use the present DSA-110 sample of localized FRBs to first explore the characteristics of the host galaxies. In Section 4.2 below, we focus on the star formation histories as probes of the formation of FRB progenitors via the delay time distribution (DTD).

The basic properties of the host galaxies of the DSA-110 sample, and the FRB sightlines through these galaxies, are not unusual with respect to the existing sample of localized FRBs (e.g., Gordon et al. 2023). The left panel of Figure 5 shows the flux ratios of nebular emission lines observed from the DSA-110 hosts in a Baldwin–Phillips–Terlevich (BPT) diagram (Baldwin et al. 1981). Most measurements and constraints on the line ratios are consistent with nebular emission driven by star formation activity, and we see no compelling evidence for AGN contributions. We note that 20220319D is more consistent with line ratios seen in LINER galaxies, although that line ratio was measured directly on the nucleus of the (well resolved) galaxy (Ravi et al. 2023b). Despite line ratios consistent with ionization by star formation, we found that SED modeling was improved by the inclusion of AGN terms; IR

colors are particularly sensitive to the presence of AGN (Leja et al. 2018).

The right panel of Figure 5 compares the published and present sample of FRBs to a model of DM from the intergalactic medium. The median redshift of the DSA-110 sample is 0.24. A typical analysis assumes $DM = DM_{\text{ISM,MW}} + DM_{\text{halo,MW}} + DM_{\text{IGM}} + DM_{\text{host}}/(1+z)$. This equation explains the DM-redshift relationship (“Macquart relation”) when DM_{IGM} is evaluated based on the mean baryon density over the path length to the FRB redshift, z . There are four DSA-110 FRBs with more than 200 pc cm^{-3} excess DM (20220307B, 20220825A, 20220914A, 20221012A). In the case of 20220914A, this is directly attributed to the intracluster gas associated with the host galaxy (Connor et al. 2023). Contributions from intervening structures (e.g., filaments, groups) for other DSA-110 FRBs will be discussed in more detail in L. Connor et al. (2024, in preparation).

Useful morphological information is only accessible for a handful of DSA-110 hosts. As discussed by Ravi et al. (2023b), the host of 20220319D is a face-on barred spiral and the FRB is significantly offset. The disk-dominated host galaxy of 20220207C is viewed nearly edge-on, and a significant $DM_{\text{IGM}} + DM_{\text{host}}/(1+z) = 170 \text{ pc cm}^{-3}$ is observed (assuming $DM_{\text{halo,MW}} = 10 \text{ pc cm}^{-3}$) despite the low redshift of 0.043. Detailed morphological analysis will be presented in K. Sharma et al. (2024, in preparation).

Important insight can be gained from an analysis of the total stellar mass and recent star formation rates (SFRs) of the FRB host galaxy sample. Figure 4 shows the stellar mass and SFR for both the published and DSA-110 FRB host galaxies in three redshift bins. The SFRs are averaged over the last 100 Myr from a nonparametric star formation history analysis. For reference, we used the largest field galaxy sample modeled using similar techniques (COSMOS; Leja et al. 2020), following Gordon et al. (2023), and the published FRB hosts were also analyzed using similar techniques. The DSA-110 sample spans 2 orders of magnitude in both stellar mass and SFR, and 3 orders of magnitude in specific SFR. This diversity of host properties is consistent with the published FRB sample.

The DSA-110 sample is subject to a selection effect on optical magnitude. For example, using *kcorrect* (Blanton & Roweis 2007), we estimate the characteristic galaxy that is detectable in PS1 (5σ stack limits). For galaxies with mass-to-light ratios from 0.7–1, we find minimum stellar masses, $M_{\odot,\text{min}}$ of $8 \times 10^8 M_{\odot}$ at $z=0.1$, $9 \times 10^9 M_{\odot}$ at $z=0.3$, and $4 \times 10^{10} M_{\odot}$ at $z=0.6$. This selection effect is clear in Figure 4. While the minimum stellar mass of a DSA-110 host excludes dwarf galaxies, the present sample is sensitive to the star-forming main sequence and quiescent galaxies in all redshift bins.

Figure 4 shows the distribution of mass and SFR for published and DSA-110 host galaxies. Early analysis of FRB hosts (Heintz et al. 2020; Bhandari et al. 2022) seemed to distinguish FRB hosts from the star-forming main sequence and quiescent galaxy population (Schawinski et al. 2014). However, newer FRB host modeling analysis that uses nonparametric star formation histories shows no such distinction (Leja et al. 2019; Gordon et al. 2023). Figure 4 confirms that FRB host galaxies are associated with star-forming and quiescent hosts, which dominate the field galaxy population by number and stellar mass.

A new result from the DSA-110 FRB host galaxy sample is the identification of massive hosts with low specific SFRs (as

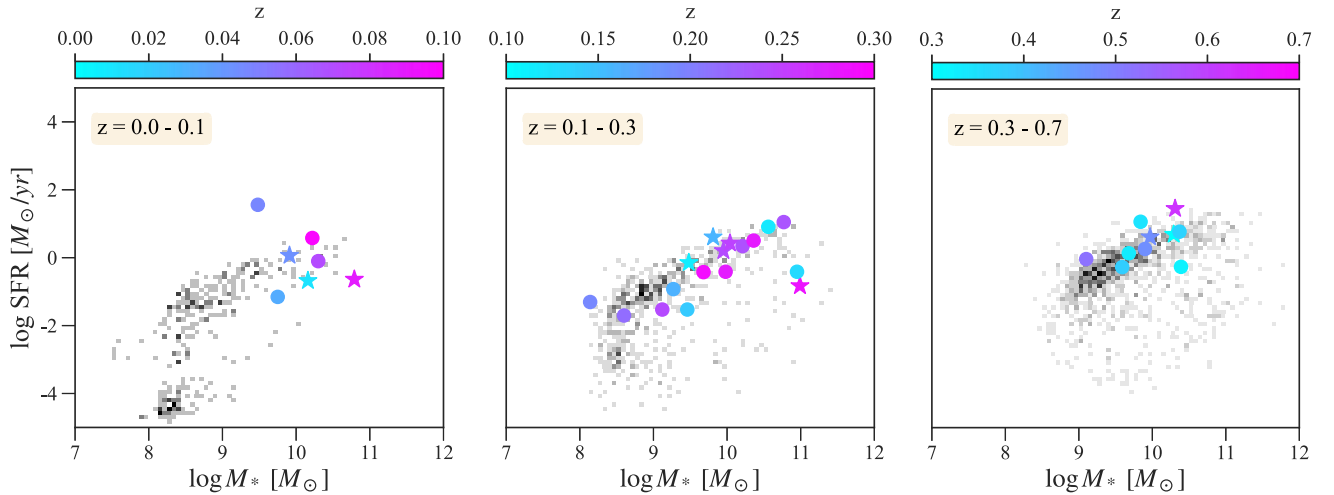


Figure 4. Stellar mass vs. recent SFR for FRB host galaxies and COSMOS galaxies in three redshift bins, 0–0.1, 0.1–0.3, and 0.3–0.7 (Laigle et al. 2016). The background color shows the number density of galaxies, which is dominated by the star-forming sequence. The FRB hosts marked by circles were presented in Gordon et al. (2023), and hosts marked by stars were discovered by DSA-110 and are presented here. The color map for the symbols shows the redshift of the FRB host galaxy.

parameterized in, e.g., Speagle et al. 2014). Two of the 11 hosts in our sample (20220509G, 20221012A) are massive, low-SFR galaxies with high mass-weighted stellar ages. However, the significance of the quiescent hosts is only meaningful when considered relative to the incidence of star-forming hosts. The fact that the DSA-110 hosts are a magnitude-limited sample means that we can test this significance statistically.

Figure 6 shows the cumulative distribution of the hosts in stellar mass, in comparison with the cumulative distributions of stellar mass and SFR of the background galaxy population. The background galaxy population was obtained from the COSMOS sample modeled with *Prospector* and Leja et al. (2020) using selections identical to the PS1 magnitude limits for the FRB host sample. Roughly half of the star formation in the Universe is contributed by galaxies that contribute only 15%–30% of its stellar mass (for $z < 0.7$). That distinction, and how it evolves with redshift, allows us to associate FRB formation with specific environments by comparing mass distributions. If FRB occurrence is tied to either current or the accumulation of past star formation, we expect the stellar mass distribution to trace that of star formation or stellar mass, respectively. Despite the presence of massive, quiescent hosts, the DSA-110 hosts tend to follow the cumulative SFR distribution in both redshift bins. This is consistent with previous FRB host distributions and FRB rate analyses that attribute FRB formation to recent star formation (Bochenek et al. 2021; James et al. 2022; Gordon et al. 2023).

More detailed insight can be gained by associating the occurrence of FRBs with specific stellar population ages via a DTD, as described below.

4.2. DTD

FRBs and other transients are produced by sources that are born during periods of star formation. Galaxies that are actively forming stars are associated with short-lived sources (e.g., core-collapse SNe; Cappellaro et al. 2015), while early-type galaxies are more likely to be associated with long-lived transient progenitors (Zheng & Ramirez-Ruiz 2007). The DTD describes the time between the formation of stars and transient events and

has been used to study short GRBs (Zevin et al. 2022), Type Ia supernovae (SNe Ia; Wiseman et al. 2021), and core-collapse SNe (Castrillo et al. 2021).

The DTD is used to statistically infer transient origins. For example, the minimum delay time for core-collapse SNe was initially assumed to be tied to the lifetime of massive stars ($t_d \approx 20$ –50 Myr). However, DTD analysis now supports theoretical modeling that shows binary evolution introduces a tail of $\sim 15\%$ late explosions (up to 200 Myr; Sana et al. 2012; Castrillo et al. 2021). Compact object binaries are expected to inspiral as they emit gravitational radiation, producing a DTD power-law slope of $\beta = -1$. For comparison, short GRBs have a delay time power-law slope of $\beta = -1.83^{+0.35}_{-0.39}$ (from 200 Myr to 8 Gyr; Zevin et al. 2022) and for SNe Ia $\beta = -1.13^{+0.04}_{-0.06}$ (assuming $t_{\min} = 40$ Myr; Wiseman et al. 2021).

For the present host galaxy sample, we model the DTD as a power law with a minimum, maximum, and slope for the FRB time relative to the star formation history of each galaxy (Appendix Figures 10 and 11; first described in Sharma et al. 2023). The probability of detecting an FRB is assumed to follow a Poisson distribution, such that for a given host galaxy i and a star formation history posterior sample j , the expected rate of FRBs is \dot{n}_i^j at redshift z_i . FRB repetition seems to violate the assumption that the delay time is calculated for a single, cataclysmic event. However, FRB source models predict activity on relatively short timescales ($< 10^6$ yr; Margalit et al. 2020; Kremer et al. 2023) or with rapid decay power law (< -2 ; Yang & Zhang 2021) compared to the typical delay times and slopes. In this case, the chance of discovering an FRB is a reasonable estimate of the maximum of its burst rate (modulated by the potential for obscuration by surrounding material). Therefore, we argue that the discovery date can be treated as a one-off event for DTD purposes.

Figure 7 shows the DTD of the current FRB host galaxy sample compared to that of other transient classes. The minimum and maximum delay time is constrained to be 110^{+250}_{-20} Myr and $6.7^{+4.56}_{-4.15}$ Gyr, respectively, and a slope of $\beta = -1.93^{+1.10}_{-0.71}$. The posterior distribution requires some chance of long delay times, which supports the conclusions of

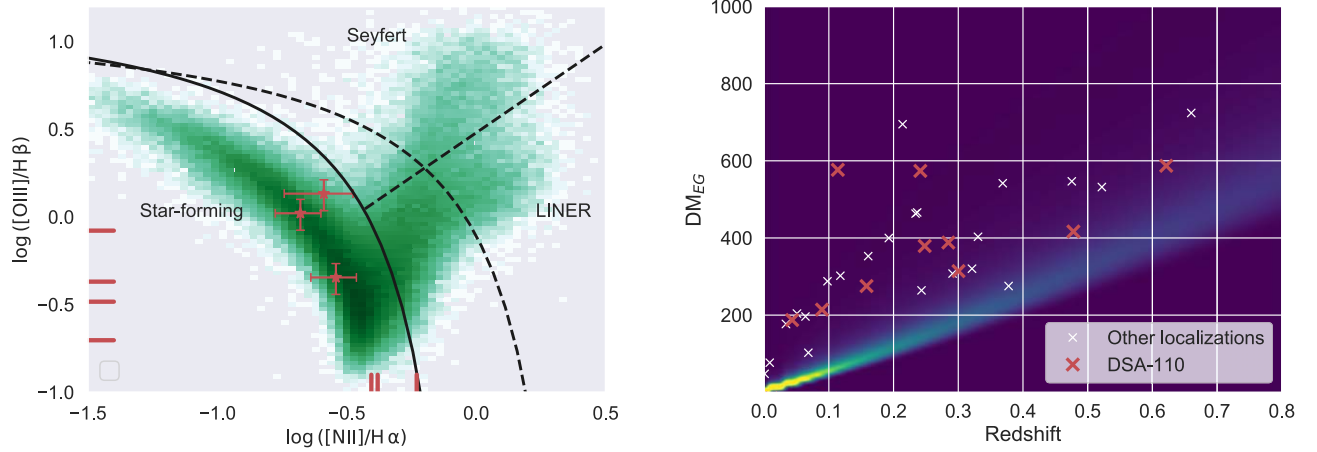


Figure 5. (Left) BPT diagram of nebular emission from DSA-110 host galaxies plotted over line ratios measured for field galaxies in the Sloan Digital Sky Survey. The solid line shows the boundary on star formation ionization (Kauffmann et al. 2003), the linear dashed line shows the LINER/Seyfert boundary (Cid Fernandes et al. 2010), and the dashed curved line shows the theoretical star formation boundary defined in Kewley et al. (2001). Three DSA-110 host galaxies have all four transitions measured and seven have a single line ratio measured. The latter are shown as red lines at the edge of the plot. 20220509G has no detected emission lines and is not shown. (Right) Extragalactic DM for FRBs compared to the probability density of DM from the intergalactic medium vs. redshift. The DSA-110 FRB sample is shown with cyan stars and published events with white crosses. We use the FRB code with function `prob_dmz.grid_P_DMcosmic_z` with $\beta=3.0$ and $F=0.31$.

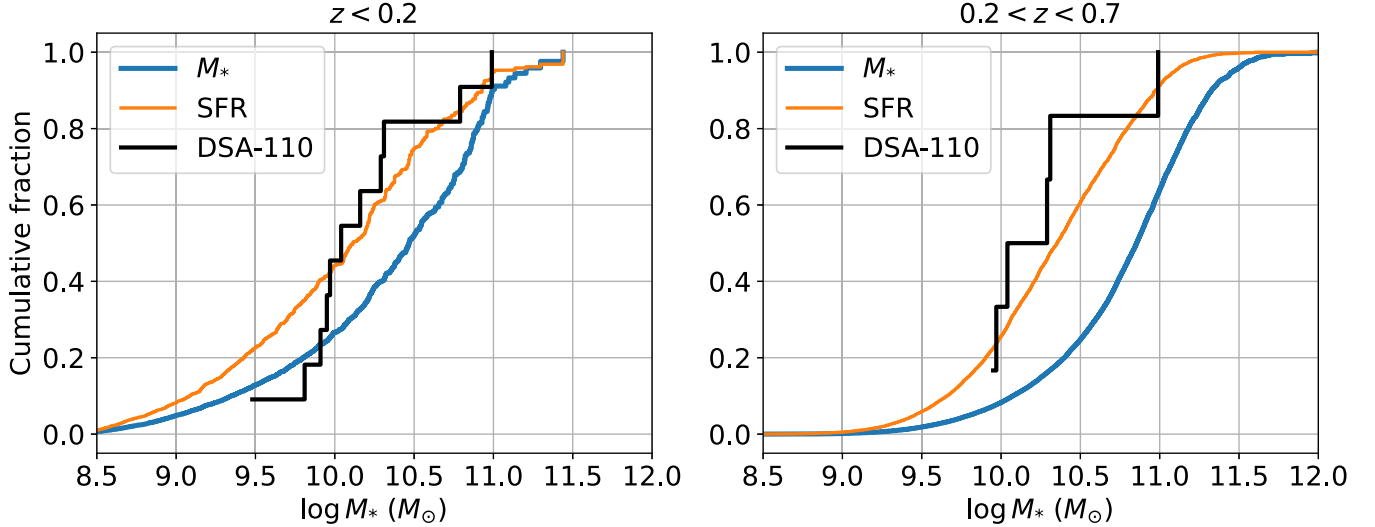


Figure 6. The cumulative fraction of stellar mass (M_* ; blue curves), SFR (orange curves), and DSA-110 FRBs (black curves) contributed by galaxies above a given stellar mass. Data are shown in two redshift intervals ($z < 0.2$ and $0.2 < z < 0.7$) that evenly split the number of DSA-110 FRBs. The background galaxy sample is from the COSMOS field Leja et al. (2020), analyzed using identical techniques to the DSA-110 FRB hosts. We have applied the same magnitude limits ($r < 23.2$ and $i < 23.1$) in the DSA-110 sample to the COSMOS sample.

Sharma et al. (2023). While the FRB host sample is small, it looks similar to that of the short GRB DTD under our assumption of a power-law DTD.

An important caveat to this analysis is that we assume a single, stationary Poisson process for the entire FRB population. In fact, there may be multiple kinds of FRB. For these reasons, the slope of the DTD power law should not be directly compared to that of other DTDs. The minimum and maximum of the distribution are likely robust to these caveats. However, we expect the estimate of t_{\min} to be affected by the lack of data constraining recent star formation history for some hosts.

Despite these caveats, the DTD analysis provides useful context to the binary framing of whether FRB hosts trace star formation or stellar mass. We find FRBs can occur with either a short (~ 100 Myr) or long ($\gtrsim 2$ Gyr) delay from star formation.

This could be interpreted as a single FRB population with a power law spanning a range of delay times or multiple populations and an overall rate dominated by short delay times. Some modeling of the larger sample of FRB DMs and redshifts show that the rate evolves with redshift similarly to the mean SFR of the Universe, which is consistent with the association of FRBs to mostly star-forming hosts in the present and previous samples (Lu & Piro 2019; Bochenek et al. 2021; James et al. 2022). Alternatively, analysis of the DM-implied distance distribution of CHIME/FRB discoveries suggests formation via a delayed channel, which is consistent with the wide DTD measured here (Hashimoto et al. 2020; Zhang & Zhang 2022). It should eventually be possible to resolve this tension through deviations of the evolution of the FRB rate from that of star formation, which scales as $(1+z)^{2.7}$ in the Local Universe. Specifically, long delays shift the rate peak to later times and

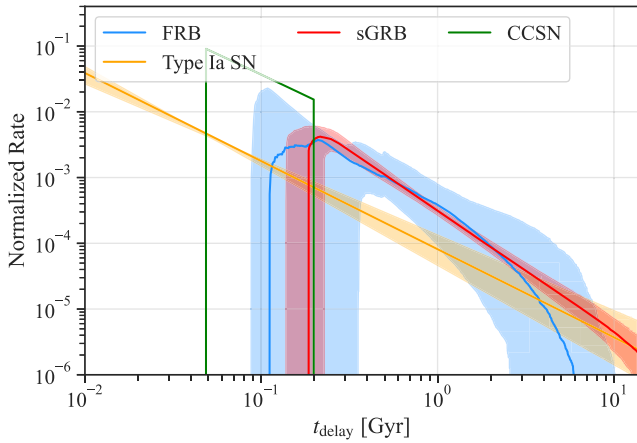


Figure 7. Delay time distributions for galaxies relative to transients discovered in them. The blue line shows our DSA-110 FRB sample, the red line shows short GRBs (Zevin et al. 2022), the green line shows core-collapse SNe (Zapartas et al. 2017), and the yellow line shows SNe Ia (Heringer et al. 2019). The FRB DTD is measured nonparametrically from the star formation history distributions presented here (see also Sharma et al. 2023).

flatten its evolution. This is evident in other transient populations with wide DTDs, such as SNe Ia and short GRBs (Greggio et al. 2008; Zevin et al. 2022).

5. Conclusions

We have presented a sample of 11 FRBs discovered by DSA-110 and selected them based on their association with host galaxies. This represents the largest and most uniform sample of FRB host galaxies. The FRBs are not known to repeat and are fainter and narrower in time than previous large FRB samples. Despite that, the bursts are phenomenologically similar to previous FRB discoveries from wide-field survey telescopes, such as CHIME and ASKAP. The new host galaxy sample supports prior work in associating FRBs with galaxies with active star formation. However, we find a wide DTD for FRBs relative to star formation.

The wide DTD requires that at least some sources of FRBs are formed over a wide range of times relative to star formation. Binary or dynamical formation channels (e.g., Margalit et al. 2019; Kremer et al. 2021) are particularly attractive because they can form over a range of delays and naturally explain some burst phenomenology, such as periodic activity cycles. It remains difficult to distinguish between the single and multiple FRB formation channels because burst properties only weakly correlate with environmental properties. With this new sample, we strengthen the evidence for repeating FRBs to be associated with PRS, which, if true, suggests that activity is causally related to the PRS' emission.

The DSA-110 continues to detect FRBs and associate them with host galaxies. Future DSA-110 publications will use large, uniform samples of burst spectra and polarization to classify sources and characterize their environments. Larger host galaxy samples will include morphological and offset analysis that can test formation channels. It may eventually be possible to detect enough hosts to model the FRB rate with multiple formation channels, as has been done for SNe Ia (Sullivan et al. 2006). Furthermore, FRB localization samples are still small, such that any effects or subclasses that occur in less than 1% of the population remain to be discovered.

Acknowledgments

We thank the OVRO staff for making this science possible through epidemics, fires, floods, and other disasters. The observatory is located on the ancestral homelands of the Big Pine Paiute Tribe of the Owens Valley. We recognize and acknowledge the historical and cultural significance of these lands to members of the tribe.

The DSA-110 is supported by the National Science Foundation Mid-Scale Innovations Program in Astronomical Sciences (MSIP) under grant AST-1836018. Some of the data presented herein were obtained at the W. M. Keck Observatory, which is operated as a scientific partnership among the California Institute of Technology, the University of California, and the National Aeronautics and Space Administration (NASA). The Observatory was made possible by the generous financial support of the W. M. Keck Foundation.

Some of the data presented herein were obtained at the W. M. Keck Observatory, which is operated as a scientific partnership among the California Institute of Technology, the University of California, and NASA. The Observatory was made possible by the generous financial support of the W. M. Keck Foundation. The authors wish to recognize and acknowledge the very significant cultural role and reverence that the summit of Maunakea has always had within the indigenous Hawaiian community. We are most fortunate to have the opportunity to conduct observations from this mountain.

We acknowledge use of the VLA calibrator manual and the radio fundamental catalog. This research has made use of NASA's Astrophysics Data System.

The Pan-STARRS1 Surveys (PS1) and the PS1 public science archive have been made possible through contributions by the Institute for Astronomy, the University of Hawaii, the Pan-STARRS Project Office, the Max-Planck Society and its participating institutes, the Max Planck Institute for Astronomy, Heidelberg and the Max Planck Institute for Extraterrestrial Physics, Garching, The Johns Hopkins University, Durham University, the University of Edinburgh, the Queen's University Belfast, the Harvard-Smithsonian Center for Astrophysics, the Las Cumbres Observatory Global Telescope Network Incorporated, the National Central University of Taiwan, the Space Telescope Science Institute, the NASA under grant No. NNX08AR22G issued through the Planetary Science Division of the NASA Science Mission Directorate, the National Science Foundation grant No. AST-1238877, the University of Maryland, Eotvos Lorand University (ELTE), the Los Alamos National Laboratory, and the Gordon and Betty Moore Foundation.

The Legacy Surveys consist of three individual and complementary projects: the Dark Energy Camera Legacy Survey (DECaLS; Proposal ID #2014B-0404; PIs: David Schlegel and Arjun Dey), the Beijing-Arizona Sky Survey (BASS; NOAO Prop. ID #2015A-0801; PIs: Zhou Xu and Xiaohui Fan), and the Mayall z-band Legacy Survey (MzLS; Prop. ID #2016A-0453; PI: Arjun Dey). DECaLS, BASS, and MzLS together include data obtained, respectively, at the Blanco telescope, Cerro Tololo Inter-American Observatory, NSF's NOIRLab; the Bok telescope, Steward Observatory, University of Arizona; and the Mayall telescope, Kitt Peak National Observatory, NOIRLab. Pipeline processing and analyses of the data were supported by NOIRLab and the Lawrence Berkeley National Laboratory (LBNL). The Legacy Surveys project is honored to be permitted to conduct

astronomical research on Iolkam Du’ag (Kitt Peak), a mountain with particular significance to the Tohono O’odham Nation.

This research uses services or data provided by the Astro Data Lab at NSF’s National Optical-Infrared Astronomy Research Laboratory. NOIRLab is operated by the Association of Universities for Research in Astronomy (AURA) under a cooperative agreement with the National Science Foundation. LBNL is managed by the Regents of the University of California under contract to the U.S. Department of Energy.

The Legacy Surveys imaging of the DESI footprint is supported by the Director, Office of Science, Office of High Energy Physics of the U.S. Department of Energy under contract No. DE-AC02-05CH1123, by the National Energy Research Scientific Computing Center, a DOE Office of Science User Facility under the same contract; and by the U.S. National Science Foundation, Division of Astronomical Sciences under contract No. AST-0950945 to NOAO.

Facilities: Hale, VLA, Keck:I (LRIS), Keck:II (ESI), DSA-110, PS1

Software: Astropy (Astropy Collaboration et al. 2013, 2018, 2022), astroquery (Ginsburg et al. 2019), astropath (Aggarwal et al. 2021), emcee (Foreman-Mackey et al. 2013), lpipe (Perley 2019), Prospector (Johnson et al. 2021), CASA (CASA Team et al. 2022), Heimdall (Barsdell 2012), wsclean (Offringa et al. 2014), dynesty v2.1.0 (Speagle 2020), Bilby (Ashton et al. 2019; Romero-Shaw et al. 2020), FRB (Prochaska et al. 2023).

Appendix Spectroscopy and Spectral Modeling

Table 4 summarizes the photometric and spectroscopic measurements made for the FRB host galaxies. Figures 8 and 9 show the modeling of the host galaxy photometry and spectroscopy. Figures 10 and 11 show the star-formation history for all hosts.

Table 4
Photometric and Spectroscopic Observations of the DSA-110 FRB Host Galaxy Sample

FRB Name	Photometry	Spectroscopy
20220207C	PS1 <i>grizy</i> , 2MASS <i>HK_s</i> , ALLWISE w1w2	Keck/LRIS
20220307B	PS1 <i>grizy</i> , WIRC <i>JH</i>	Hale/DBSP
20220310F	PS1 <i>riz</i>	Keck/LRIS
20220319D	PS1 <i>grizy</i> , 2MASS <i>HK_s</i> , ALLWISE w1w2	Hale/DBSP
20220418A	PS1 <i>grizy</i> , WIRC <i>JH</i>	Keck/LRIS
20220506D	PS1 <i>rizy</i> , WIRC <i>JH</i> , ALLWISE w1w2	Keck/LRIS
20220509G	PS1 <i>grizy</i> , 2MASS <i>HK_s</i> , ALLWISE w1w2	Keck/LRIS ^a
20220825A	PS1 <i>grizy</i>	Keck/LRIS ^a
20220914A	PS1 <i>grizy</i>	Keck/LRIS ^a
20220920A	PS1 <i>grizy</i>	Hale/DBSP
20221012A	PS1 <i>grizy</i> , 2MASS <i>HK_s</i> , ALLWISE w1w2	Keck/LRIS ^a

Note.

^a Observed with the blue side.

Table 5
Host Galaxy Line Fluxes for Four Transitions Used in the BPT Diagram (Figure 5)

FRB Name	H α	H β	[O III] 5007	[N II] 6584
20220207C	8.65×10^{-16}	5.11×10^{-17}	$5(1) \times 10^{-17}$	$1.81(7) \times 10^{-16}$
20220307B	$5.9(1) \times 10^{-15}$	$2.3(1) \times 10^{-15}$
20220310F	8.924×10^{-17}	1.93×10^{-17}	$2.6(4) \times 10^{-17}$	$2.3(6) \times 10^{-17}$
20220319D ^a	$2.00(3) \times 10^{-14}$	$1.46(4) \times 10^{-14}$
20220418A	...	4.89×10^{-17}	$2.1(5) \times 10^{-17}$...
20220506D	1.18×10^{-16}	4.98×10^{-18}	...	$4.9(5) \times 10^{-17}$
20220509G ^b
20220825A	...	$1.23(3) \times 10^{-16}$	$4.0(2) \times 10^{-17}$...
20220914A	...	$9.0(2) \times 10^{-17}$	$7.5(2) \times 10^{-17}$...
20220920A	1.08×10^{-15}	3.41×10^{-16}	$1.5(3) \times 10^{-16}$	$3.1(1) \times 10^{-16}$
20221012A	...	$1.00(4) \times 10^{-16}$	$2.0(3) \times 10^{-17}$...

Notes. Line fluxes are not corrected for Galactic or host extinction.

^a Lines measured in the nucleus of the host given in Ravi et al. (2023a; see also Ravi et al. 2023b).

^b No emission lines detected, but redshift measured from absorption lines.

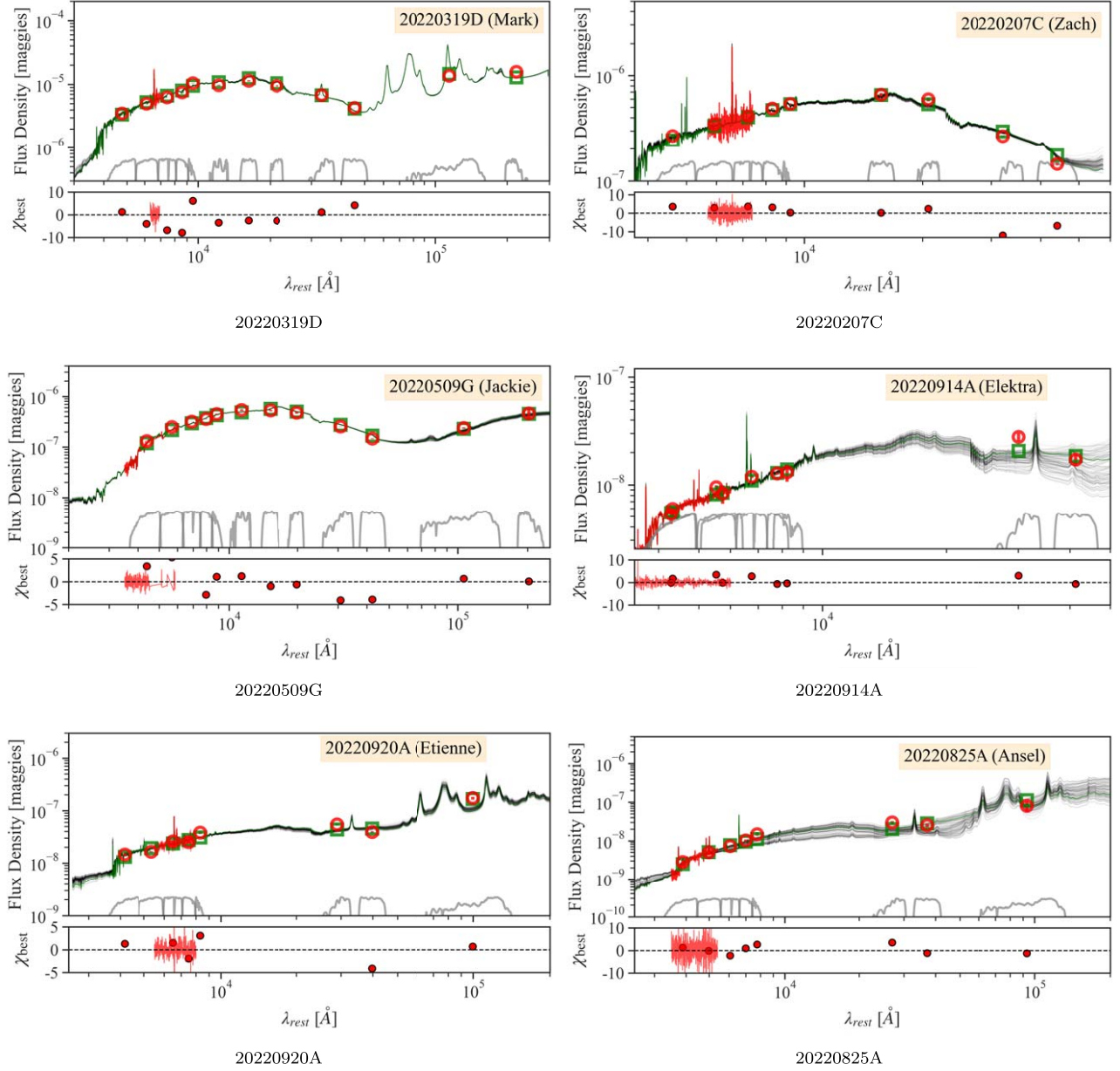
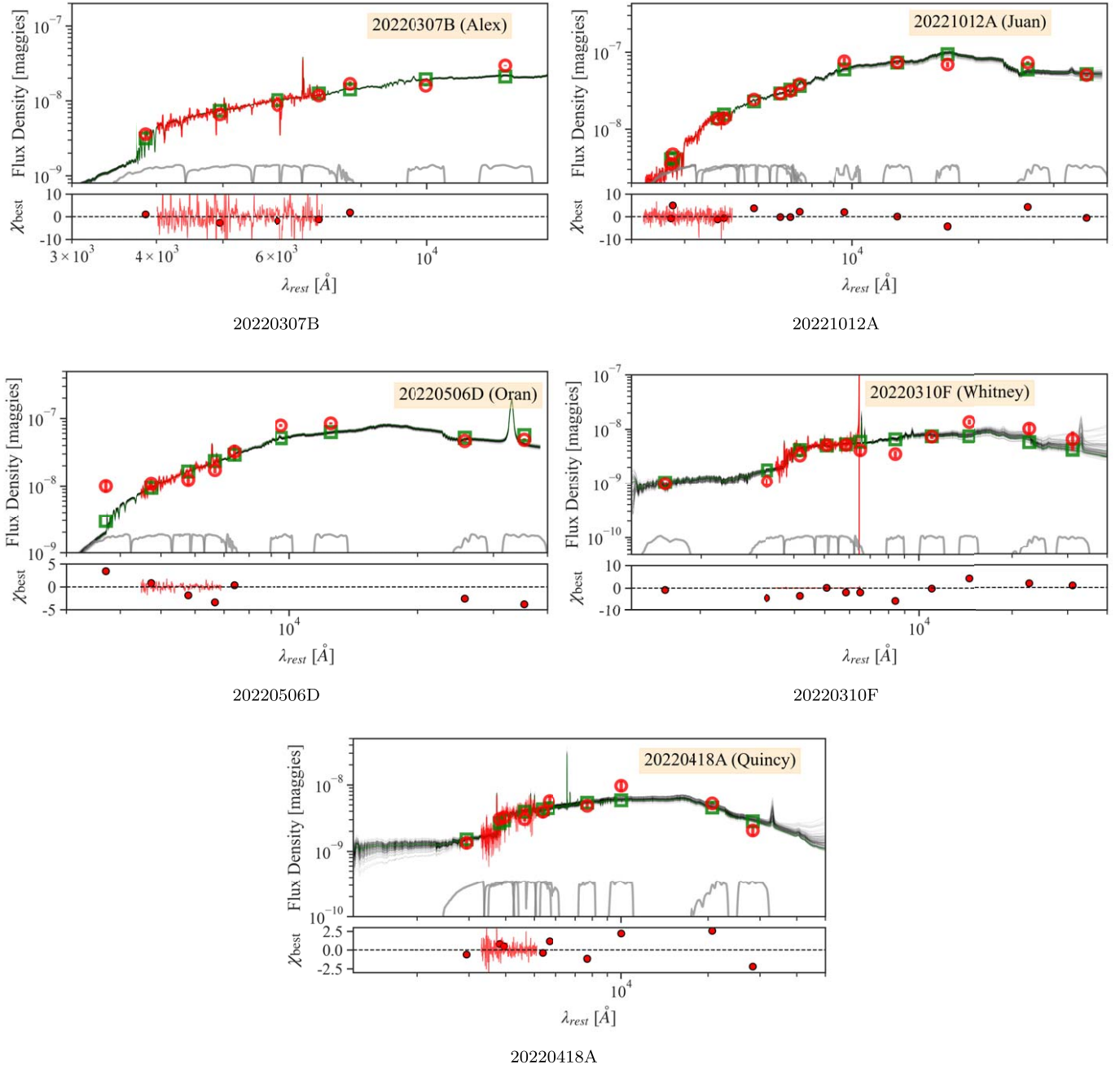


Figure 8. Optical and IR SED for FRB host galaxies (part 1 of 2). Each figure has two panels with measurements, model, and bandpasses in the top and residuals in the bottom. The top panel shows measurements in red, the best model values at the wavelength/band of the measurement in green, and bandpasses in gray. Black lines show a set of random models drawn from the best posterior model distribution. The top right of each figure shows the reduced chi-square of the best model fit.

**Figure 9.** Optical and IR SED for FRB host galaxies (part 2 of 2).

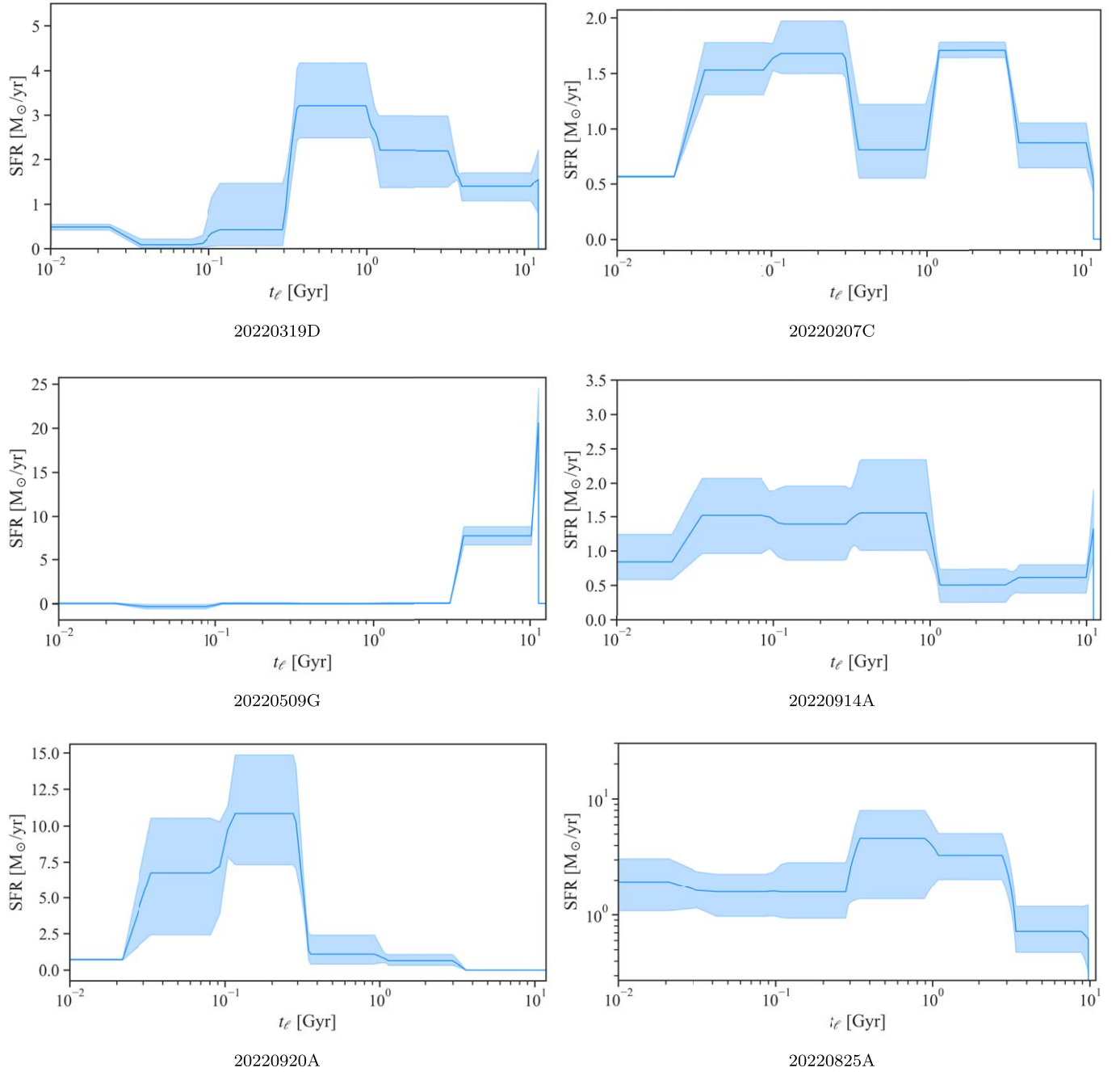
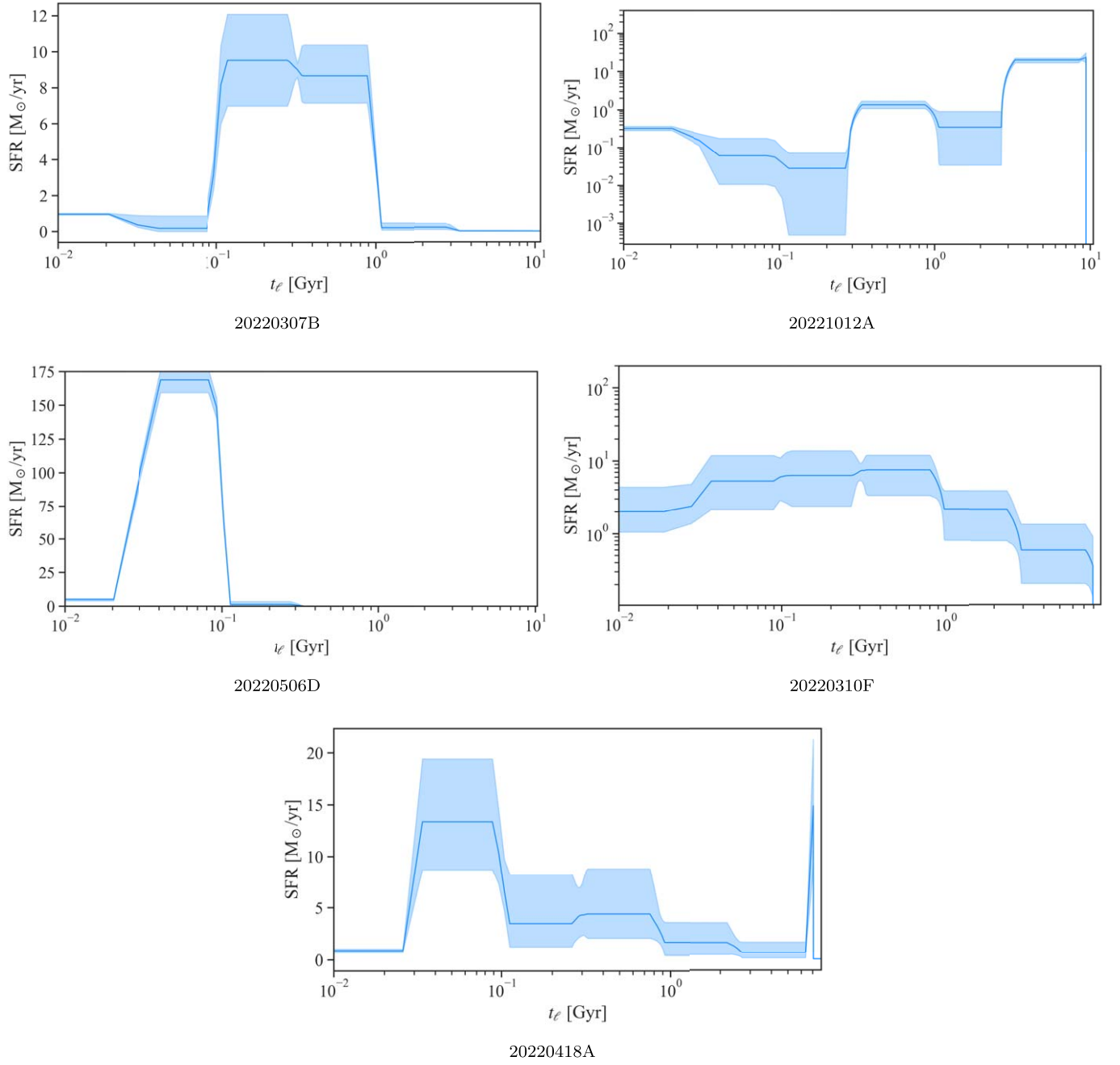






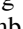
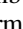







Figure 10. Star formation history for FRB host galaxies (part 1 of 2). Prospector modeling (Section 3.2) uses seven logarithmically spaced bins with a continuity prior that favors smoother changes in SFR between bins.

**Figure 11.** Star formation history for FRB host galaxies (part 2 of 2).

ORCID iDs

Casey J. Law  <https://orcid.org/0000-0002-4119-9963>
 Kritti Sharma  <https://orcid.org/0000-0002-4477-3625>
 Vikram Ravi  <https://orcid.org/0000-0002-7252-5485>
 Ge Chen  <https://orcid.org/0000-0003-2867-4544>
 Liam Connor  <https://orcid.org/0000-0002-7587-6352>
 Gregg Hallinan  <https://orcid.org/0000-0002-7083-4049>
 Greg Hellbourg  <https://orcid.org/0000-0002-8191-3885>
 James W. Lamb  <https://orcid.org/0000-0002-5959-1285>
 Myles B. Sherman  <https://orcid.org/0000-0002-6573-7316>
 Jun Shi  <https://orcid.org/0000-0003-1647-7762>
 Dana Simard  <https://orcid.org/0000-0002-8873-8784>
 Reynier Squillace  <https://orcid.org/0000-0001-6748-5290>
 Nitika Yadlapalli Yurk  <https://orcid.org/0000-0003-3255-4617>

References

- Aggarwal, K., Budavári, T., Deller, A. T., et al. 2021, *ApJ*, 911, 95
- Anna-Thomas, R., Connor, L., Dai, S., et al. 2023, *Sci*, 380, 599
- Ashton, G., Hübner, M., Lasky, P. D., et al. 2019, *ApJS*, 241, 27
- Astropy Collaboration, Price-Whelan, A. M., Lim, P. L., et al. 2022, *ApJ*, 935, 167
- Astropy Collaboration, Price-Whelan, A. M., Sipőcz, B. M., et al. 2018, *AJ*, 156, 123
- Astropy Collaboration, Robitaille, T. P., Tollerud, E. J., et al. 2013, *A&A*, 558, A33
- Baldwin, J. A., Phillips, M. M., & Terlevich, R. 1981, *PASP*, 93, 5
- Barsdell, B. R. 2012, PhD thesis, Swinburne Univ. Technology
- Berger, E. 2014, *ARA&A*, 52, 43
- Bhandari, S., Heintz, K. E., Aggarwal, K., et al. 2022, *AJ*, 163, 69
- Blanton, M. R., & Roweis, S. 2007, *AJ*, 133, 734
- Bochenek, C. D., Ravi, V., Belov, K. V., et al. 2020, *Natur*, 587, 59
- Bochenek, C. D., Ravi, V., & Dong, D. 2021, *ApJL*, 907, L31
- Caleb, M., Driessen, L. N., Gordon, A. C., et al. 2023, *MNRAS*, 524, 2064
- Cappellari, M. 2017, *MNRAS*, 466, 798
- Cappellari, M. 2023, *MNRAS*, 526, 3273
- Cappellaro, E., Botticella, M. T., Pignata, G., et al. 2015, *A&A*, 584, A62
- CASA Team, Bean, B., Bhatnagar, S., et al. 2022, *PASP*, 134, 114501
- Castrillo, A., Ascasibar, Y., Galbany, L., et al. 2021, *MNRAS*, 501, 3122
- Chambers, K. C., Magnier, E. A., Metcalfe, N., et al. 2016, arXiv:1612.05560
- Chatterjee, S., Law, C. J., Wharton, R. S., et al. 2017, *Natur*, 541, 58
- Chibueze, J. O., Caleb, M., Spitler, L., et al. 2022, *MNRAS*, 515, 1365
- Chime/FRB Collaboration, Amiri, M., Andersen, B. C., et al. 2020a, *Natur*, 582, 351
- CHIME/FRB Collaboration, Amiri, M., Andersen, B. C., et al. 2021, *ApJS*, 257, 59
- Chime/FRB Collaboration, Andersen, B. C., Bandura, K., et al. 2023, *ApJ*, 947, 83
- CHIME/FRB Collaboration, Andersen, B. C., Bandura, K. M., et al. 2020b, *Natur*, 587, 54
- Cid Fernandes, R., Stasińska, G., Schlickmann, M. S., et al. 2010, *MNRAS*, 403, 1036
- Condon, J. J., Cotton, W. D., Greisen, E. W., et al. 1998, *AJ*, 115, 1693
- Connor, L., Ravi, V., Catha, M., et al. 2023, *ApJL*, 949, L26
- Cordes, J. M., & Chatterjee, S. 2019, *ARA&A*, 57, 417
- Cordes, J. M., & Lazio, T. J. W. 2002, astro, arXiv:astro-ph/0207156
- Cutri, R. M., Wright, E. L., Conrow, T., et al. 2021, yCat, II/328y
- Dey, A., Schlegel, D. J., Lang, D., et al. 2019, *AJ*, 157, 168
- Driessen, L. N., Barr, E. D., Buckley, D. A. H., et al. 2024, *MNRAS*, 527, 3659
- Evans, I. N., Primini, F. A., Miller, J. B., et al. 2020, AAS Meeting 235, 154.05
- Foreman-Mackey, D., Hogg, D. W., Lang, D., & Goodman, J. 2013, *PASP*, 125, 306
- Ginsburg, A., Sipőcz, B. M., Brasseur, C. E., et al. 2019, *AJ*, 157, 98
- Gordon, A. C., Fong, W.-f., Kilpatrick, C. D., et al. 2023, *ApJ*, 954, 80
- Graham, A. W., & Driver, S. P. 2005, *PASA*, 22, 118
- Greggio, L., Renzini, A., & Daddi, E. 2008, *MNRAS*, 388, 829
- Gregory, P. C., Scott, W. K., Douglas, K., & Condon, J. J. 1996, *ApJS*, 103, 427
- Hashimoto, T., Goto, T., On, A. Y. L., et al. 2020, *MNRAS*, 498, 3927
- Heintz, K. E., Prochaska, J. X., Simha, S., et al. 2020, *ApJ*, 903, 152
- Heringer, E., Pritchett, C., & van Kerkwijk, M. H. 2019, *ApJ*, 882, 52
- Intema, H. T., Jagannathan, P., Mooley, K. P., & Frail, D. A. 2017, *A&A*, 598, A78
- James, C. W., Prochaska, J. X., Macquart, J. P., et al. 2022, *MNRAS*, 510, L18
- Johnson, B. D., Leja, J., Conroy, C., & Speagle, J. S. 2021, *ApJS*, 254, 22
- Kauffmann, G., Heckman, T. M., Tremonti, C., et al. 2003, *MNRAS*, 346, 1055
- Kewley, L. J., Dopita, M. A., Sutherland, R. S., Heisler, C. A., & Trevena, J. 2001, *ApJ*, 556, 121
- Kirsten, F., Marcote, B., Nimmo, K., et al. 2022, *Natur*, 602, 585
- Kremer, K., Fuller, J., Piro, A. L., & Ransom, S. M. 2023, *MNRAS*, 525, L22
- Kremer, K., Piro, A. L., & Li, D. 2021, *ApJL*, 917, L11
- Lacy, M., Baum, S. A., Chandler, C. J., et al. 2020, *PASP*, 132, 035001
- Laigle, C., McCracken, H. J., Ilbert, O., et al. 2016, *ApJS*, 224, 24
- Lane, W. M., Cotton, W. D., van Velzen, S., et al. 2014, *MNRAS*, 440, 327
- Law, C. J., Bower, G. C., Burke-Spolaor, S., et al. 2018, *ApJS*, 236, 8
- Law, C. J., Connor, L., & Aggarwal, K. 2022, *ApJ*, 927, 55
- Leja, J., Johnson, B. D., Conroy, C., et al. 2019, *ApJ*, 877, 140
- Leja, J., Johnson, B. D., Conroy, C., & van Dokkum, P. 2018, *ApJ*, 854, 62
- Leja, J., Speagle, J. S., Johnson, B. D., et al. 2020, *ApJ*, 893, 111
- Li, D., Bilous, A., Ransom, S., Main, R., & Yang, Y.-P. 2023, *Natur*, 618, 484
- Li, D., Wang, P., Zhu, W. W., et al. 2021, *Natur*, 598, 267
- Lu, W., Beniamini, P., & Kumar, P. 2022, *MNRAS*, 510, 1867
- Lu, W., & Piro, A. L. 2019, *ApJ*, 883, 40
- Lytikov, M., Barkov, M. V., & Giannios, D. 2020, *ApJL*, 893, L39
- Macquart, J.-P., Bailes, M., Bhat, N. D. R., et al. 2010, *PASA*, 27, 272
- Mannings, A. G., Fong, W.-f., Simha, S., et al. 2021, *ApJ*, 917, 75
- Marcote, B., Nimmo, K., Hessels, J. W. T., et al. 2020, *Natur*, 577, 190
- Margalit, B., Beniamini, P., Sridhar, N., & Metzger, B. D. 2020, *ApJL*, 899, L27
- Margalit, B., Berger, E., & Metzger, B. D. 2019, *ApJ*, 886, 110
- Margalit, B., & Metzger, B. D. 2018, *ApJL*, 868, L4
- McKinven, R., Gaensler, B. M., Michilli, D., et al. 2023, *ApJ*, 951, 82
- Nimmo, K., Hessels, J. W. T., Kirsten, F., et al. 2022, *NatAs*, 6, 393
- Niu, C. H., Aggarwal, K., Li, D., et al. 2022, *Natur*, 606, 873
- Offringa, A. R., McKinley, B., Hurley-Walker, N., et al. 2014, *MNRAS*, 444, 606
- Oke, J. B., Cohen, J. G., Carr, M., et al. 1995, *PASP*, 107, 375
- Oke, J. B., & Gunn, J. E. 1982, *PASP*, 94, 586
- Pastor-Marazuela, I., van Leeuwen, J., Bilous, A., et al. 2023, *A&A*, 678, A149
- Perley, D. A. 2019, *PASP*, 131, 084503
- Perley, D. A., Fremming, C., Sollerman, J., et al. 2020, *ApJ*, 904, 35
- Petroff, E., Hessels, J. W. T., & Lorimer, D. R. 2022, *A&ARv*, 30, 2
- Planck Collaboration, Aghanim, N., Akrami, Y., et al. 2020, *A&A*, 641, A6
- Pleunis, Z., Good, D. C., Kaspi, V. M., et al. 2021, *ApJ*, 923, 1
- Prochaska, J. X., Simha, S., Almannin, et al. 2023, FRBs/FRB: Release to sync with Gordon et al. 2023, v2.0, Zenodo, doi:10.5281/zenodo.8125230
- Rajwade, K. M., Bezuidenhout, M. C., Caleb, M., et al. 2022, *MNRAS*, 514, 1961
- Ravi, V. 2019, *NatAs*, 3, 928
- Ravi, V., Catha, M., Chen, G., et al. 2023a, *ApJL*, 949, L3
- Ravi, V., Catha, M., Chen, G., et al. 2023b, arXiv:2301.01000
- Ravi, V., Law, C. J., Li, D., et al. 2022, *MNRAS*, 513, 982
- Rengelink, R. B., Tang, Y., de Bruyn, A. G., et al. 1997, *A&AS*, 124, 259
- Romero-Shaw, I. M., Talbot, C., Biscoveanu, S., et al. 2020, *MNRAS*, 499, 3295
- Ryder, S. D., Bannister, K. W., Bhandari, S., et al. 2023, *Sci*, 382, 294
- Sana, H., de Mink, S. E., de Koter, A., et al. 2012, *Sci*, 337, 444
- Sánchez-Blázquez, P., Peletier, R. F., Jiménez-Vicente, J., et al. 2006, *MNRAS*, 371, 703
- Sanidas, S., Caleb, M., Driessen, L., et al. 2018, in IAU Symp. 337, Pulsar Astrophysics the Next Fifty Years, ed. P. Weltevredet et al. (Cambridge: Cambridge Univ. Press), 406
- Schawinski, K., Urry, C. M., Simmons, B. D., et al. 2014, *MNRAS*, 440, 889
- Seebeck, J., Ravi, V., Connor, L., et al. 2021, arXiv:2112.07639
- Sharma, K., Somalwar, J., Law, C., et al. 2023, *ApJ*, 950, 175
- Shen, S., Mo, H. J., White, S. D. M., et al. 2003, *MNRAS*, 343, 978
- Sherman, M. B., Connor, L., Ravi, V., et al. 2023, *ApJL*, 957, L8
- Sherman, M. B., Connor, L., Ravi, V., et al. 2024, *ApJ*, 964, 131
- Shimwell, T. W., Tasse, C., Hardcastle, M. J., et al. 2019, *A&A*, 622, A1
- Skrutskie, M. F., Cutri, R. M., Stiening, R., et al. 2006, *AJ*, 131, 1163
- Speagle, J. S. 2020, *MNRAS*, 493, 3132
- Speagle, J. S., Steinhardt, C. L., Capak, P. L., & Silverman, J. D. 2014, *ApJS*, 214, 15
- Sullivan, M., Le Borgne, D., Pritchett, C. J., et al. 2006, *ApJ*, 648, 868

- Tachibana, Y., & Miller, A. A. 2018, [PASP](#), **130**, 128001
- Tendulkar, S. P., Bassa, C. G., Cordes, J. M., et al. 2017, [ApJL](#), **834**, L7
- van Leeuwen, J., Kooistra, E., Oostrum, L., et al. 2023, [A&A](#), **672**, A117
- Webb, N. A., Coriat, M., Traulsen, I., et al. 2020, [A&A](#), **641**, A136
- Wilson, J. C., Eikenberry, S. S., Henderson, C. P., et al. 2003, [Proc. SPIE](#), **4841**, 451
- Wiseman, P., Sullivan, M., Smith, M., et al. 2021, [MNRAS](#), **506**, 3330
- Woosley, S. E., & Bloom, J. S. 2006, [ARA&A](#), **44**, 507
- Yang, Y.-P., & Zhang, B. 2021, [ApJ](#), **919**, 89
- Zapartas, E., de Mink, S. E., Izzard, R. G., et al. 2017, [A&A](#), **601**, A29
- Zevin, M., Nugent, A. E., Adhikari, S., et al. 2022, [ApJL](#), **940**, L18
- Zhang, B. 2020, [Natur](#), **587**, 45
- Zhang, R. C., & Zhang, B. 2022, [ApJL](#), **924**, L14
- Zheng, Z., & Ramirez-Ruiz, E. 2007, [ApJ](#), **665**, 1220